IEEE Access
Multidisciplinary | Rapid Review | Open Access Journal

Received September 14, 2019, accepted December 5, 2019, date of publication December 19, 2019,
date of current version December 31, 2019.

Digital Object Identifier 10.1109/ACCESS.2019.2961006

Design Improvement for Blackbody Cavity Sensor for Continuous Measurement of Molten Steel Temperature

JIANGFENG CHENG[1,2], CHIA-FENG JUANG[2], (Fellow, IEEE), GUOHUI MEI[3], AND WEIHAI CHEN[1], (Member, IEEE)

[1]School of Automation Science and Electrical Engineering, Beihang University, Beijing 100191, China
[2]Department of Electrical Engineering, National Chung Hsing University, Taichung 402, Taiwan
[3]College of Information Science and Engineering, Northeastern University, Shenyang 110819, China

Corresponding authors: Chia-Feng Juang (cfjuang@dragon.nchu.edu.tw) and Guohui Mei (meiguohui@ise.neu.edu.cn)

This work was supported by the National Natural Science Foundation of China (NSFC) under Grants 61873051.

ABSTRACT The blackbody cavity sensor formed by two coaxial tubes has been widely used in continuous temperature measurement of molten steel. However, due to the closed bottom of the inner tube, the temperature accuracy, response time and temperature measurement stability are seriously affected. It's necessary to redesign and improve sensing mechanism of the traditional design, which involves multidisciplinary knowledge, including materials, heat and flow science. This paper proposes a virtual verification-based design improvement method for blackbody cavity sensor. After redesigning the structure of the sensor, a virtual model for the sensor is established. Through real-world experiment, it is found that for the temperature measurement accuracy, the deviation between the simulation and the real-world experimental result is less than 1.5°C, and for the stability time of temperature measurement, the simulation result has a deviation from the real-world experimental result less than 15%. This verifies the accuracy of the virtual model. On this basis, model simulation for further possible optimal structures and parameters is carried out, and the influence of different nitrogen flow rates and inner tube lengths on the temperature measurement accuracy and the stability time for temperature measurement is further analyzed.

INDEX TERMS Blackbody cavity sensor, virtual verification, design improvement.

I. INTRODUCTION

Blackbody cavity sensor for continuous temperature measurement of molten steel has been widely used in steel industry, as shown in Fig. 1(a). It consists of a cylindrical outer tube and a coaxial inner tube. [1], [2].

The sensor has the advantages of longer service life (20-40 hours), higher accuracy (measurement error $\leq \pm 3°$) [3], and lower cost which is lower than the platinum rhodium thermocouple. Its ability of continuous measurement plays an important role in optimization and control of the casting speed and the safe continuous casting production [3], [4].

The sensor adopts a coaxial casing structure. The outer tube blocks the erosion of molten steel, which is made of refractory material. The inner tube creates a clean temperature measuring cavity, which is a corundum tube closed at the bottom end [3]. However, since the molten steel temperature reaches 1470-1650°C [4], [5], in actual use, the following threes problems will occur.

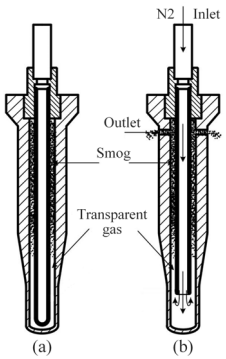

FIGURE 1. Blackbody cavity temperature sensor.

The associate editor coordinating the review of this manuscript and approving it for publication was Jenny Mahoney.

This work is licensed under a Creative Commons Attribution 4.0 License. For more information, see http://creativecommons.org/licenses/by/4.0/

(1) Due to the closed semicircle at the bottom of the corundum tube, material stress distribution is uneven, resulting in asymmetry of the corundum tube and fracture in severe cases.
(2) At high temperature, the inner corundum tube is prone to creep, causing the corundum tube to bend.
(3) There is a thermal shock problem when the tundish inserts or pulls out molten steel, which easily breaks the inner corundum tube.

To address the above problems, it is proposed to remove the semicircular bottom of inner corundum tube and appropriately shortens its length, as shown in Fig. 1(b).

But, under high temperature of molten steel, impurity, the main component of which is sodium oxide, will be evaporated from the outer Al-carbon tube. Melting point of the impurity is around 1275°C. When the temperature is higher than the melting point, the impurity is a transparent gas, which does not affect the temperature measurement. Otherwise, the impurity gas will aggregate into particles [6], blocking the optical paths and reducing the intensity of the radiation energy received by the sensor, thereby affecting the temperature measurement results. To avoid the influence of impurity on temperature measurement, nitrogen gas is blown into the sensor from the top of inner corundum tube. Meanwhile, two vent holes are drilled at the upper part of the outer Al-carbon tube to allow exhausting nitrogen and impurity. However, different nitrogen flow rates and inner tube' lengths will affect the temperature measurement accuracy and the temperature measurement stability time (MSTime).

To deeply analyze the theoretical basis and influence mechanism, the following issues need to be considered.

i. Blowing off soot particle and vapor belongs to the category of turbulent diffusion multiphase flow.
ii. The sensor is partially inserted into molten steel. So the influence of phase change on the turbulent diffusion needs to be considered, which is caused by the temperature gradient distribution in the cavity of sensor.
iii. The phase change affects radiation heat transfer, including the blocking of radiation path, the variation of the absorption and scattering coefficient.
iv. The phase change is also accompanied by endothermic and exothermic process, which affects the temperature distribution in the cavity.

The complex process involves temperature field including heat transfer, convection heat transfer, radiation heat transfer and heat transfer in phase change, and flow field including turbulent diffusion, multiphase flow and Buoyancy-driven flow. Thus, the process is more complicated.

To provide theoretical basis for design improvement of the sensor, establish an accurate virtual model and obtain optimal design parameters, this paper first proposes a virtual verification-based design improvement method. Then this paper redesigns the structure of the blackbody cavity sensor, and establishes a corresponding virtual model of the sensor, including geometry model, multi-physical field model, material physical properties and boundary conditions. Through comparison between real-world experiment and virtual simulation, the virtual model is corrected gradually until the accuracy of the virtual model is verified. Finally, based on the verified virtual model, the design improvement can be carried out through simulation, including the influence of different nitrogen flow rates and inner tube's lengths on the temperature measurement accuracy and temperature MSTime.

The remainder of the paper is organized as follows. In section II, a virtual verification-based design improvement method is proposed. In section III, a virtual model of the blackbody cavity sensor is established. To verify accuracy of the virtual model, a verification method is presented from two aspects in section IV. Based on the verified virtual model, in section V, the design improvement for the blackbody cavity sensor is carried out, which points out the possible design optimization scheme. Finally, section VI gives a succinct conclusion.

II. VIRTUAL VERIFICATION-BASED DESIGN IMPROVEMENT METHOD

In this section, a virtual verification-based design improvement method for blackbody cavity sensor is proposed, as shown in Fig. 2. The method includes the following three steps.

Step 1 (Virtual Model Establishment): As shown by the blue line in Fig. 2, the goal of this step is to build a virtual model after considering possible improvement schemes. While establishing the virtual model that has high fidelity with the physical sensor and can truly reflect it, it is necessary to construct the following four aspects [7], [8]. (i) **Geometry model**. The dimensions of the blackbody cavity sensor and each component need to be described. The dimension parameters come from the existing product or the new design scheme. (ii) **Behaviour-rule-constraint model**. This model describes the performance and behaviours of the sensor, such as input, output, operating mechanism, reaction mechanism and so on. It involves multidisciplinary knowledge including heat transfer, convection heat transfer, radiation heat transfer, turbulent diffusion, multiphase flow, phase change, and the like. (iii) **Material properties**. This model is used to describe the material properties used in various components of the sensor, such as density, hardness, specific heat capacity, standard-state enthalpy, thermal conductivity and viscosity. (iv)**Boundary conditions**. It is mainly used to describe the boundary conditions involved in the use of the sensor, such as initial temperature distribution, initial position and measuring range.

After building the virtual model, simulation computation needs to be carried out with analysis tools, such as finite element analysis and user-defined algorithms. Then the virtual model is gradually corrected through comparing the simulation results with the design expectations.

Step 2 (Virtual Simulation and Real-World Experiment): This step is shown by the green line in Fig. 2.

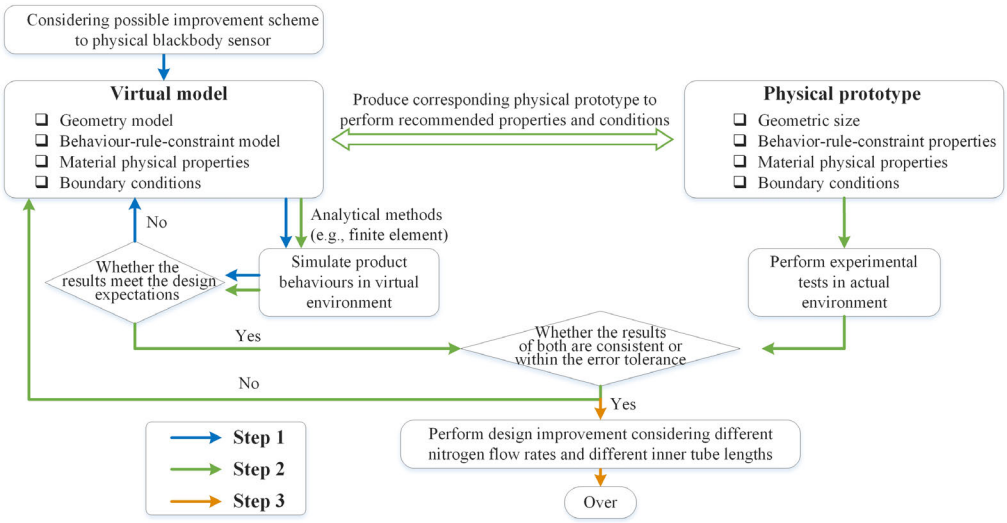

FIGURE 2. Virtual verification-based design improvement method for blackbody cavity sensor.

After considering possible improvement schemes, a physical prototype is produced. Then, on the one hand, the boundary conditions are configured in the virtual environment and simulation analysis is carried out. On the other hand, in the real-world environment, the same conditions as the virtual environment are set and the physical prototype is performed. By comparing the simulation results with the experimental results, if the results of both are consistent or the deviation between both is within the error tolerance, the virtual model is verified. If the deviation does not meet the expected value, the virtual model needs to be constantly corrected until the results meet the requirements. The virtual model is thus verified.

Step 3 (Design Improvement Based on the Verified Model): The process of this step is shown by the orange line in Fig. 2. Only if the virtual model is verified, it is possible to carry out simulation experiment to optimize design parameters. This paper sets the initial conditions and boundary conditions for the virtual simulation that are consistent with the real-world environment. Through simulation, one can make sense of the influence of different nitrogen flow rates and different inner tube's lengths on temperature measurement accuracy and MSTime. Then the final design parameters of the sensor can be determined after weighing the advantages and disadvantages in actual use.

III. VIRTUAL MODEL FOR BLACKBODY CAVITY SENSOR

A. GEOMETRY MODEL

The structure of the sensor is as shown in Fig. 1(b), as well as the movement of nitrogen and impurity. The portion of the fixing tube and the outer tube above the vent holes are not established in geometry model, as shown in Fig. 3(a), because the upper part of the sensor is above the molten steel, and its temperature distribution has little effect on sensor's temperature measurement accuracy and MSTime. The geometry model consists of the solid region, i.e., outer Al-carbon tube and inner corundum tube, and the fluid region, i.e., internal cavity surrounded by the two tubes.

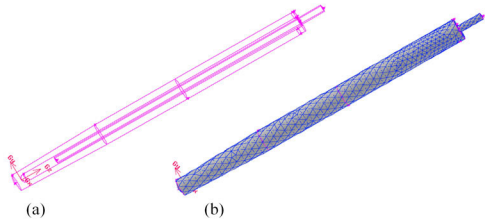

FIGURE 3. Geometry model of blackbody cavity sensor.

The constructed geometry model needs to be meshed, as shown in Fig. 3(b). In this research, meshing of the geometric model is performed in Gambit software, which has several methods for evaluating mesh quality, such as Aspect Ratio, Diagonal Ratio, Edge Ratio, EquiAngle Skew, EquiSize Skew, MidAngle Skew, Size Change, etc. Three more important and popular methods are chosen to evaluate the mesh quality, including EquiSize Skew, EquiAngle Skew, and Size Change.

a) EquiSize Skew is the skewness calculated by the cell size. In general, EquiSize Skew is between 0 and 1, with 0 being the best quality and 1 being the worst quality. The EquiSize Skew value of this structure is below 0.6, the EquiSize Skew of more than 90% of the meshes is below 0.5.
b) EquiAngle Skew calculates the skewness by the cell angle, between 0 and 1, with 0 being the best quality and 1 being the worst quality. The EquiAngle Skew value of this structure is below 0.6.
c) Size Change refers to the ratio of adjacent cell sizes, only for 3D cells, preferably within 2. The Size Change value of this structure is below 2

With the evaluation of above three methods, the mesh quality of this structure is acceptable from the engineering viewpoint, which can meet the subsequent calculation requirements.

B. MULTI-PHYSICAL FIELD MODEL

1) HEAT CONDUCTION AND CONVECTION HEAT TRANSFER MODEL

a: HEAT TRANSFER AND CONVECTION HEAT TRANSFER MODEL FOR FLUID REGIONS AND FLUID-SOLID REGIONS [9]

Heat transfer model between nitrogen, soot vapor and the solid regions of the cavity is established as follows:

$$\frac{\partial}{\partial t}(\rho E) + \nabla \cdot (\vec{v}\rho E) = \nabla \cdot \left(k_{eff}\nabla T - \sum h_j \vec{J}_j\right) \quad (1)$$

Heat transfer model for soot particle phase in the fluid region is established as follows:

$$\frac{\partial}{\partial t}(\rho E) + \nabla \cdot (\vec{v}\rho E) = \nabla \cdot \left(k_{eff}\nabla T - \sum h_j \vec{J}_j\right) + S_{\mathrm{h}} \quad (2)$$

where $k_{eff}\nabla T$ and $\sum h_j \vec{J}_j$ represent the energy transfer caused by heat conduction and component diffusion, respectively. E represents the total energy of the fluid micelle, i.e., the sum of internal energy and kinetic energy, is given by

$$E = \sum_j Y_j \int_{T_{ref}}^{T} c_{p,j} dT + \frac{v^2}{2} \quad (3)$$

For convection heat transfer, the Buoyancy-driven flow needs to be considered. The density of the substance needs to be set to a temperature-dependent function $\rho = f(T)$. The material parameters' function expression of nitrogen, soot particle and soot vapor can be found in [6], [10], [11].

b: HEAT TRANSFER MODEL FOR SOLID REGIONS [9]

The outer wall of the Al-carbon tube under molten steel and the wall of the inner corundum tube have heat sources S_h, and the heat transfer model is as follows:

$$\frac{\partial}{\partial t}(\rho h) = \nabla \cdot (k_s \nabla T) + S_h \quad (4)$$

There is no heat source in other parts of the solid regions, and the heat transfer model can be simplified as

$$\frac{\partial}{\partial t}(\rho h) = \nabla \cdot (k_s \nabla T) \quad (5)$$

where the thermal conductivity k_s of the inner and outer tubes is isotropic, and can be set as a scalar constant.

2) RADIATION HEAT TRANSFER MODEL

The sensor is worked under high temperature around 1800K, and radiation heat transfer plays an extremely important role. The Discrete Ordinates (DO) radiation model is adopted considering the optical thickness $(a + \sigma_s)s$, the scattering of soot particles and the effect of soot particles on radiation.

TABLE 1. Notation used throughout the paper.

Notation	Description
k_{eff}	Effective thermal conductivity
$\vec{J}_j$	Diffusion flux of component j
h_j	Sensible enthalpy of component j
T, ∇T	Temperature, temperature difference
ρ	Density
E	Energy of the fluid micelle
$\vec{v}$	Velocity field
S_h	Volumetric heat source
Y_j	Mass fraction of component j
$c_{p,j}$	Specific heat of component j
T_{ref}	Reference temperature 298.15K
$\vec{r}$	Position vector
$\vec{s}$	Direction vector
$\vec{s}'$	Scattering direction vector
s	Path length
a	Absorption coefficient
n	Refractive index
σ_s	Scattering coefficient
I	Radiation intensity
Φ	Phase function
Ω'	Solid angle
λ	Radiation wavelength
a_λ	Spectral absorption coefficient
$I_{b\lambda}$	Blackbody radiation intensity
σ	Stefan-Boltzmann constant (5.672×10^{-8} W/m^2-K^4)
ε_{pn}	Emissivity of the n^{th} particle
A_{pn}	Projected area of the n^{th} particle
T_{pn}	Temperature of the n^{th} particle
f_{pn}	Scattering factor of the n^{th} particle
f_d	Diffusion coefficient
ε_w	Wall emissivity
T_w	Wall temperature
k	Kinetic energy
ε	Dissipation rate of kinetic energy k
$\alpha_k, \alpha_\varepsilon$	Turbulent Prandtl numbers of the k and ε equation
G_k, G_b	Turbulence kinetic energy generated by the mean Velocity gradients and Buoyancy
g_i	The component of gravity in direction of i
u_i	Velocity components
S_k, S_ε	User-defined source terms
μ_{eff}	Effective viscosity
μ_q	Shear viscosity of phase q
λ_q	Bulk viscosity of phase q
$\vec{F}_q$	External body force
$\vec{F}_{lift,q}$	Lift force
$\vec{F}_{vm,q}$	Virtual mass force
K_{pq}	Momentum exchange coefficient between phases(= K_{qp})
P	Pressure shared by all phases
α_q	Volume ratio of the q^{th} phase
$\vec{v}_q$	Velocity of the q^{th} phase
$\vec{q}_q$	Heat flux of q^{th} phase
Q_{pq}	Intensity of heat exchange between the p^{th} and q^{th} phase, Q_{pq}=-Q_{qp}
h_{pq}	Interphase enthalpy between the p^{th} and q^{th} phase.
τ_p	Particle relaxation time
e_{ss}	Coefficient of restitution for particle collisions
Θ_s	Particle Temperature
$g_{0,\ ss}$	Radial distribution function for collision probability
d_s	Particle diameter

Gray-band radiation model is used to simulate non-gray radiation. Based on the spectral intensity $I_\lambda(\vec{r}, \vec{s})$, the radiation transfer equation is as follows [12], [13]:

$$\nabla \cdot (I_\lambda(\vec{r}, \vec{s})\vec{s}) + (a + \sigma_s) I_\lambda(\vec{r}, \vec{s}) = a_\lambda n^2 I_{b\lambda} + \frac{\sigma_s}{4\pi}\int_0^{4\pi} I_\lambda(\vec{r}, \vec{s})\,\Phi(\vec{s}, \vec{s}')\,d\Omega' \quad (6)$$

The scattering coefficient, scattering phase function and refractive index are considered to be wavelength independent.

The non-gray DO radiation model divides the entire radiation spectral band into N bands and integrates the wavelengths over all wavelength ranges, thus obtaining a transport equation about $I_\lambda \Delta\lambda$. Radiation heat transfer is contained within each band $\Delta\lambda$. Within each band, it is considered to be blackbody radiation, and its blackbody radiation in unit solid angle is as

$$[F(0 \to n\lambda_2 T) - F(0 \to n\lambda_1 T)]\, n^2 \frac{\sigma T^4}{\pi} \tag{7}$$

where $F(0 \to n\lambda T)$ is the blackbody radiation in the range of $0 \sim \lambda$ wavelength at temperature T under the medium of refractive index n, and λ_1, λ_2 are the boundaries of the band.

The blackbody cavity sensor in this research belongs to full-wave radiation. At any temperature in the cavity, the ratio of the radiation intensity of all wavelengths to the radiation intensity of the absolute blackbody at the corresponding wavelength is fixed. Therefore, it is regarded as gray radiation, that is, the emissivity is constant.

In actual use, soot particles will be evaporated from the outer tube, which block the radiation paths. The soot particles also have a scattering effect while absorbing part of the radiation energy. Therefore, the effect of particles on radiation must be considered while calculating radiation heat transfer.

In the radiation transfer equation, the effect of the particle phase [12]–[14] is expressed as

$$\begin{aligned}\nabla \cdot (I\vec{s}) + (a + a_p + \sigma_p) I(\vec{r}, \vec{s}) \\ = an^2 \frac{\sigma T^4}{\pi} + E_p + \frac{\sigma_p}{4\pi} \int_0^{4\pi} I(\vec{r}, \vec{s}')\Phi(\vec{s}, \vec{s}')d\Omega'\end{aligned} \tag{8}$$

where E_p, a_p, and σ_p are the equivalent emission, equivalent absorption coefficient and equivalent scattering coefficient of soot particles, respectively. They are defined as follows:

$$E_p = \lim_{V \to 0} \sum_{n=1}^{N} \varepsilon_{pn} A_{pn} \frac{\sigma T_{pn}^4}{\pi V} \tag{9}$$

$$a_p = \lim_{V \to 0} \sum_{n=1}^{N} \varepsilon_{pn} \frac{A_{pn}}{V} \tag{10}$$

$$\sigma_p = \lim_{V \to 0} \sum_{n=1}^{N} \left(1 - f_{pn}\right) \left(1 - \varepsilon_{pn}\right) \frac{A_{pn}}{V} \tag{11}$$

where the summation $\sum$ is performed on all N soot particles in volume V.

The inner walls of the sensor cavity belong to the opaque surfaces. When the radiation hits the surfaces, specular reflection and diffuse reflection will occur. The walls absorb some of the energy, while also radiates energy outward, which is related to the emissivity. Fig. 4 shows the radiation mechanism of the inner surfaces of the sensor [15], [16].

The expressions of wall emission energy, diffuse reflected energy, specular reflection energy and absorbed radiant energy in Fig. 4 are given as follows [15], [16]:

$$q_e = n^2 \varepsilon_w \sigma T_w^4 \tag{12}$$

$$q_{dr} = f_d \left(1 - \varepsilon_w\right) q_{in} \tag{13}$$

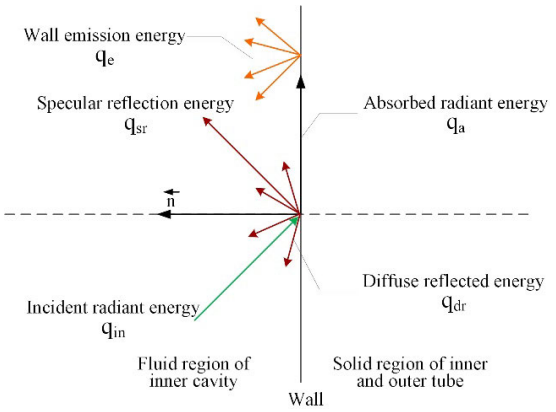

FIGURE 4. Radiation mechanism of the inner wall.

$$q_{sr} = \left(1 - f_d\right)\left(1 - \varepsilon_w\right) q_{in} \tag{14}$$

$$q_a = \varepsilon_w q_{in} \tag{15}$$

The incident radiant energy q_{in} of the inner wall of the cavity is as

$$q_{in} = \int_{\vec{s}\cdot\vec{n}>0} I_{in}\vec{s} \cdot \vec{n} d\Omega \tag{16}$$

The net radiant energy q_{out} leaving the wall is as follows:

$$q_{out} = \left(1 - \varepsilon_w\right) q_{in} + n^2 \varepsilon_w \sigma T_w^4 \tag{17}$$

For all $\vec{s}$ leaving the wall, the radiation intensity of the wall is as follows:

$$I_o = \frac{q_{out}}{\pi} \tag{18}$$

3) TURBULENCE MODEL

In this paper, the nitrogen flow rates are set to 0.25-2.5m^3/h. The Reynolds number is between 1000∼4000. Moreover, due to the complex geometry, the fluid flow in the cavity is considered to be a fully developed turbulence.

In the cavity of the sensor, there is no vortex, rotation and rapid change of tension during the blowing process of soot under the forced convection. The RNG $k - \varepsilon$ model is economical and reasonable, and has a wide range of applications. The model has undergone practical tests of numerous engineering fluid problems and is relatively reliable. Therefore, this model [17]–[19] will be used as given below.

$$\begin{aligned}\frac{\partial}{\partial t}(\rho k) + \frac{\partial}{\partial x_i}(\rho k u_i) \\ = \frac{\partial}{\partial x_j}\left(\alpha_k \mu_{eff} \frac{\partial k}{\partial x_j}\right) + G_k + G_b - \rho\varepsilon + S_k\end{aligned} \tag{19}$$

$$\begin{aligned}\frac{\partial}{\partial t}(\rho \varepsilon) + \frac{\partial}{\partial x_i}(\rho \varepsilon u_i) \\ = \frac{\partial}{\partial x_j}\left(\alpha_\varepsilon \mu_{eff} \frac{\partial \varepsilon}{\partial x_j}\right) \\ + C_{1\varepsilon}\frac{\varepsilon}{k}\left(G_k + C_{3\varepsilon} G_b\right) - C_{2\varepsilon}^* \rho \frac{\varepsilon^2}{k} + S_\varepsilon\end{aligned} \tag{20}$$

where α_k and α_ε are defined below where $\alpha_0 = 1.0$:

$$\left|\frac{\alpha - 1.3929}{\alpha_0 - 1.3929}\right|^{0.6321}\left|\frac{\alpha + 2.3929}{\alpha_0 + 2.3929}\right|^{0.3679} = \frac{\mu_{mol}}{\mu_{eff}} \quad (21)$$

and $C_{1\varepsilon} = 1.42$, $C_{2\varepsilon} = 1.68$, and the expression of $C^*_{2\varepsilon}$ is as follows:

$$C^*_{2\varepsilon} \equiv C_{2\varepsilon} + \frac{C_\mu \eta^3 (1 - \eta/\eta_0)}{1 + \beta\eta^3} \quad (22)$$

and G_k is given by

$$G_k = -\rho\overline{u_i' u_j'}\frac{\partial u_j}{\partial x_i} \quad (23)$$

The established energy exchange model needs to consider the influence of Buoyancy-driven flow. Similarly, Buoyancy-driven flow also has an effect on turbulence. G_b in (19) and (20) is given by

$$G_b = \beta g_i \frac{\mu_t}{\mathrm{Pr}_t}\frac{\partial T}{\partial x_i} \quad (24)$$

where $\mathrm{Pr}_t = 1/\alpha$ is the Prandtl number. α can be calculated from (21), where $\alpha_0 = 1/\mathrm{Pr} = k/\mu c_p$, and β is defined as

$$\beta = -\frac{1}{\rho}\left(\frac{\partial \rho}{\partial T}\right)_p \quad (25)$$

It can be seen from the k equation that Buoyancy enhances turbulence kinetic energy in the unstable layer and suppresses turbulence in the stable layer. In the ε equation, the effect of Buoyancy on turbulence is reflected in the constant $C_{3\varepsilon}$, which is calculated by the following equation:

$$C_{3\varepsilon} = \tanh\left|\frac{v}{u}\right| \quad (26)$$

where v is the component of the fluid velocity in the direction of gravity, and u is the component of the fluid velocity in the direction perpendicular to the direction of gravity.

4) MULTIPHASE FLOW AND INTERPHASE EXCHANGE MODEL

There is a phase change between soot particle and soot vapor in the cavity of the sensor. So, the Euler-Euler approach for multiphase flow is used to model this process, instead of the Euler-Lagrange approach which is only suitable for tracking inert particles. In the Euler-Euler approach, the Eulerian model is used based on the following three reasons. First, the Eulerian model is more accurate than the Mixture model. Second, the concentration of the soot in the upper cavity of the corundum tube is very low, while the concentration below the bottom of the inner corundum tube is relatively concentrated. Finally, the drag model between each phase is relatively clear and more suitable for the Eulerian model.

a: MOMENTUM CONSERVATION EQUATION

The momentum conservation equation of Eulerian model is as follows:

$$\begin{aligned}&\frac{\partial}{\partial t}\left(\alpha_q\rho_q\vec{v}_q\right) + \nabla\cdot\left(\alpha_q\rho_q\vec{v}_q\vec{v}_q\right)\\ &\quad= -\alpha_q\nabla p + \nabla\cdot\bar{\bar{\tau}}_q\\ &\qquad+\alpha_q\rho_q\vec{g} + \left(\vec{F}_q + \vec{F}_{lift,q} + \vec{F}_{vm,q}\right)\\ &\qquad+\sum_{p=1}^{n}\left(K_{pq}(\vec{v}_p - \vec{v}_q) + \dot{m}_{pq}\vec{v}_{pq} - \dot{m}_{qp}\vec{v}_{qp}\right)\end{aligned} \quad (27)$$

where p and q stands for the two different phases, $\vec{v}_{pq}$ is the interphase velocity ($\dot{m}_{pq} > 0$ denotes the transfer mass from phase p to phase q, $\vec{v}_{pq} = \vec{v}_p$; $\dot{m}_{pq} < 0$ denotes the transfer mass from phase q to phase p, $\vec{v}_{pq} = \vec{v}_q$), and the same principle applies to $\dot{m}_{qp}$. In addition, $\bar{\bar{\tau}}_q$ is the q^{th} phase stress-strain tensor, and given by

$$\bar{\bar{\tau}}_q = \alpha_q\mu_q\left(\nabla\vec{v}_q + \nabla\vec{v}_q^T\right) + \alpha_q\left(\lambda_q - {}^2\!/_3\mu_q\right)\nabla\cdot\vec{v}_q\bar{\bar{I}} \quad (28)$$

The $\vec{F}_{lift,q}$ is often applied in occasions where the velocity gradient changes greatly, such as the swirling flow. For small particle fluid, the lift is negligible compared with the drag force. Obviously, the influence of lift can be ignored in this research. For the $\vec{F}_{vm,q}$, it is suitable for the second phase particle acceleration motion, and its density is much smaller than the main phase. In this research, the density of soot particle is much larger than nitrogen, so the virtual mass force is not considered.

With regard to the momentum equation of nitrogen phase, we note that nitrogen is the main phase, which is fluid and has no phase change, so there is no mass transfer. Its momentum conservation equation [20] is given as

$$\begin{aligned}&\frac{\partial}{\partial t}\left(\alpha_n\rho_n\vec{v}_n\right) + \nabla\cdot\left(\alpha_n\rho_n\vec{v}_n\vec{v}_n\right)\\ &\quad= -\alpha_n\nabla p + \nabla\cdot\bar{\bar{\tau}}_n\\ &\qquad+\alpha_n\rho_n\vec{g} + \vec{F}_n + \sum_{p=1}^{n}K_{nn}\left(\vec{v}_p - \vec{v}_n\right)\end{aligned} \quad (29)$$

where ϕ_n represents the nitrogen-related parameters.

With regard to the momentum equations of soot particle and vapor phase, it is noted that there is a phase change between the soot particle phase and the soot vapor phase. The momentum conservation equations of soot particle and soot vapor are shown as follows [20], [21]:

$$\begin{aligned}&\frac{\partial}{\partial t}\left(\alpha_s\rho_s\vec{v}_s\right) + \nabla\cdot\left(\alpha_s\rho_s\vec{v}_s\vec{v}_s\right)\\ &\quad= -\alpha_s\nabla p - \nabla p_s + \nabla\cdot\bar{\bar{\tau}}_s + \alpha_s\rho_s\vec{g} + \vec{F}_s\\ &\qquad+\sum_{g=1}^{n}\left(K_{gs}(\vec{v}_g - \vec{v}_s) + \dot{m}_{gs}\vec{v}_{gs} - \dot{m}_{sg}\vec{v}_{sg}\right)\end{aligned} \quad (30)$$

$$\begin{aligned}&\frac{\partial}{\partial t}\left(\alpha_g\rho_g\vec{v}_g\right) + \nabla\cdot\left(\alpha_g\rho_g\vec{v}_g\vec{v}_g\right)\\ &\quad= -\alpha_g\nabla p + \nabla\cdot\bar{\bar{\tau}}_g + \alpha_g\rho_g\vec{g} + \vec{F}_g\\ &\qquad+\sum_{s=1}^{n}\left(K_{sg}(\vec{v}_s - \vec{v}_g) + \dot{m}_{sg}\vec{v}_{sg} - \dot{m}_{gs}\vec{v}_{gs}\right)\end{aligned} \quad (31)$$

where ϕ_s and ϕ_g represent the related parameters of the soot particle and soot vapor.

b: MASS CONSERVATION EQUATION

The mass conservation equation in the Eulerian model is defined for the volume fraction of each phase [20], as shown below.

$$\frac{\partial}{\partial t}\left(\alpha_q \rho_q\right) + \nabla \cdot \left(\alpha_q \rho_q \vec{v}_q\right) = \sum_{p=1}^{n}\left(\dot{m}_{pq} - \dot{m}_{qp}\right) \quad (32)$$

In other words, for the nitrogen phase, soot particle phase and soot vapor phase, the mass conservation equations are only slightly different, except that the nitrogen phase has no mass transfer.

c: ENERGY CONSERVATION EQUATION

The energy conservation equation in the Eulerian model [20], [22] is shown as:

$$\begin{aligned}\frac{\partial}{\partial t}\left(\alpha_q \rho_q h_q\right) &+ \nabla \cdot \left(\alpha_q \rho_q \vec{u}_q h_q\right) \\ &= \alpha_q \frac{\partial p_q}{\partial t} + \bar{\bar{\tau}}_q : \nabla \vec{u}_q \\ &\quad - \nabla \vec{q}_q + S_q + \sum_{p=1}^{n}\left(Q_{pq} + \dot{m}_{pq} h_{pq} - \dot{m}_{qp} h_{qp}\right) \quad (33)\end{aligned}$$

Similarly, for the three phases mentioned above, the energy conservation equations are slightly different. There is no energy transfer caused by mass transfer in the energy equation of the nitrogen phase. That is, there are no the items of $\dot{m}_{pq}h_{pq}$ and $\dot{m}_{qp}h_{qp}$.

d: INTERPHASE EXCHANGE COEFFICIENT

The momentum exchange between each phase is based on the exchange coefficient K_{qp} [23] and is defined as follows:

$$K_{pq} = \frac{\alpha_p \rho_p f}{\tau_p} \quad (34)$$

$$\tau_p = \frac{\rho_p d_p^2}{18\mu_q} \quad (35)$$

Specifically, the drag model f between nitrogen and soot particles adopts the Syamlal-O'Brien model [24], which is not given here. The Schiller and Naumann model [25] is used for the drag model between nitrogen and soot vapor, and between soot vapor and soot particles.

e: VISCOSITY MODEL OF SOOT PARTICLE

During the transfer and collision of soot particles, the momentum exchange between particles is affected by bulk viscosity [26] which is shown in (36), and shear viscosity which includes collisional viscosity [27] and kinetic viscosity [28], as shown in (37) and (38). The concentration of soot particle in this research is very low, so the shear viscosity does not include the frictional viscosity.

$$\lambda_s = \frac{4}{3}\alpha_s \rho_s d_s g_{0,ss}\left(1 + e_{ss}\right)\left(\frac{\Theta_s}{\pi}\right)^{1/2} \quad (36)$$

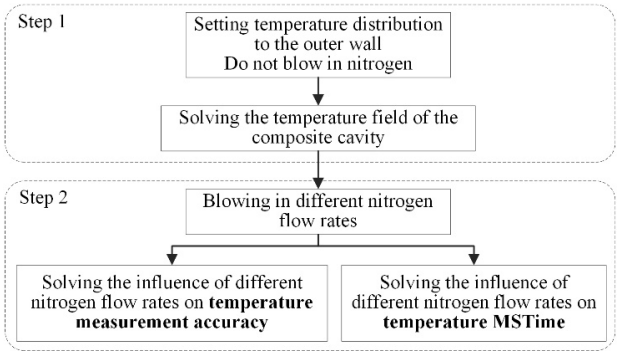

FIGURE 5. Overall simulation solution strategy.

$$\mu_{s,col} = \frac{4}{5}\alpha_s \rho_s d_s g_{0,ss}\left(1 + e_{ss}\right)\left(\frac{\Theta_s}{\pi}\right)^{1/2} \quad (37)$$

$$\mu_{s,kin} = \frac{\alpha_s d_s \rho_s \sqrt{\Theta_s \pi}}{6(3 - e_{ss})}\left[1 + \frac{2}{5}\left(1 + e_{ss}\right)\left(3e_{ss} - 1\right)\alpha_s g_{0,ss}\right] \quad (38)$$

$$\mu_s = \mu_{s,col} + \mu_{s,kin} \quad (39)$$

f: HEAT EXCHANGE MODEL BETWEEN EACH PHASE

In the process of interaction between the three phases, nitrogen, soot particle and soot vapor in the cavity also have heat exchange with each other, which can be considered as a function of the temperature difference between different phases [20].

$$Q_{pq} = h_{pq}\left(T_p - T_q\right) \quad (40)$$

where $h_{pq} = (h_{qp})$ is related to the Nusselt number N_{u_p} of the p phase.

$$h_{pq} = \frac{6k_q \alpha_p \alpha_q N_{u_p}}{d_p^2} \quad (41)$$

where $k_q$is the thermal conductivity of the q^{th} phase. And the Nusselt number N_{u_p} differs depending on the properties of different phases.

IV. VIRTUAL MODEL VERIFICATION WITH EXPERIMENT AND SIMULATION

Accuracy of the virtual model needs to be verified and continuously corrected until the accuracy satisfies the expected target. Here, accuracy of the virtual model is verified from two perspectives, i.e., temperature measurement accuracy (as shown in part A, section IV) and temperature MSTime (as shown in part B, section IV).

The computation solution for the virtual model is performed in Fluent software tool, and the solution strategy is illustrated in Fig. 5, including two steps. **Step 1**. Without considering the heat transfer, turbulence, phase transition and radiation caused by nitrogen and impurity, only setting the temperature distribution of outer wall of the outer tube, the simulation computation is performed until the temperature distribution of the sensor reaches a stable

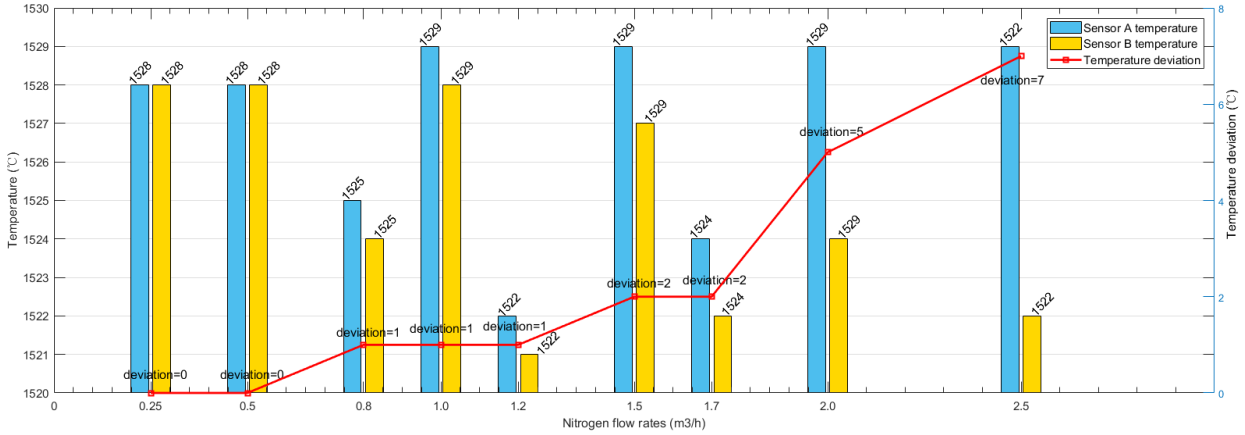

FIGURE 6. Temperature deviation under different nitrogen flow rates under real-world experiment.

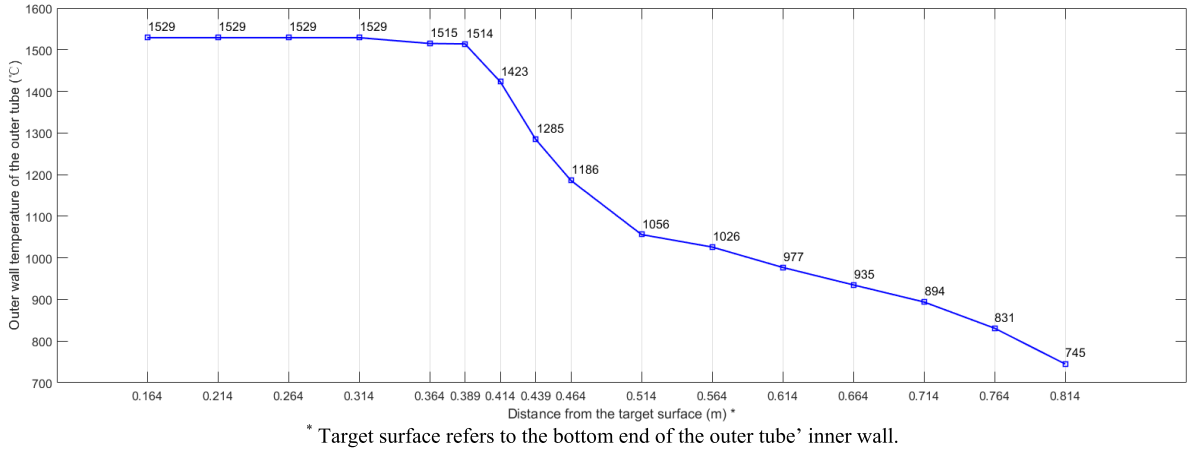

* Target surface refers to the bottom end of the outer tube' inner wall.

FIGURE 7. Initial temperature distribution setting for the outer wall of the outer tube for simulation.

state. **Step 2**. Nitrogen with different flow rates is blown into the cavity. When the simulation reaches a new stable state, the influence of different nitrogen flow rates on the temperature measurement accuracy is analyzed. In addition, the influence of different nitrogen flow rates on MSTime also needs to be investigated to verify the virtual model.

A. VIRTUAL VERIFICATION FROM TEMPERATURE MEASUREMENT ACCURACY

The verification method from the perspective of temperature measurement accuracy is shown as verification method 1.

The reasons for the temperature deviation of 1.5°C are as follows. Blackbody cavity sensor for molten steel mainly works in the range of 1400-1600°C, and has been widely used in steel production. It is declared in the public data that the temperature measurement accuracy is ±3°C [3], but the real accuracy can reach ±1.5°C. Therefore, it is relatively reasonable to set the deviation between simulation and real-world experiment to 1.5°C.

Verification method 1	
Real-world experiment	
Setting:	Sensor A with closed bottom of inner tube is used to measure the true molten steel temperature without blowing nitrogen. Sensor B_i are inserted the same tundish with sensor A, and are blown into nitrogen with flow rates of 0.25, 0.5, 0.8, 1.0, 1.2, 1.5, 1.7, 2.0 and 2.5 (m^3/h). When A and B_i are stable, the measurement values of sensor A and B_i are recorded at the same time. (T_{Ai}, T_{Bi}), i=1,2, …, 7
Output:	Temperature deviations: $\Delta T_i=T_{Ai}-T_{Bi}$, i=1,2, …, 7
Simulation experiment	
Setting:	Seven groups of experiment are carried out with nitrogen flow rates of 0.25, 0.5, 0.8, 1.0, 1.2, 1.5, 1.7, 2.0 and 2.5 (m^3/h).
Output:	Simulation temperature deviations: $\Delta T_i'$, i=1,2, …, 7
Verification	
1	If ($\Delta T=\lvert\Delta T_i-\Delta T_i'\rvert < 1.5$°C)
2	The accuracy of model is verified.
3	Else
4	The accuracy of model is not verified.

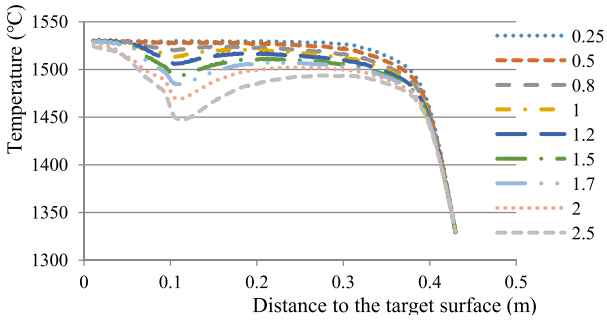

FIGURE 8. Temperature distributions of the inner wall of the outer tube under different nitrogen flow rates obtained by simulation.

TABLE 2. The emissivity of the whole cavity under different flow rates.

Flow rates (m^3/h)	Material emissivity	Target surface temperature (K)	Cavity emissivity	Temperature deviation (°C)
0.25	0.7	1804.12	0.999261366	0.3
0.5	0.7	1804.08	0.999122977	0.4
0.8	0.7	1803.87	0.998502544	0.7
1.0	0.7	1803.57	0.997683021	1.0
1.2	0.7	1803.69	0.997919967	0.9
1.5	0.7	1803.37	0.996959406	1.4
1.7	0.7	1803.17	0.996349635	1.6
2.0	0.7	1800.84	0.990217233	4.4
2.5	0.7	1797.75	0.981344126	8.4

1) REAL-WORLD EXPERIMENT

As shown in verification method 1, sensor A and B_i are inserted into the same tundish and measured simultaneously. The temperature measurement values of sensor A are the true molten steel temperature. Meanwhile, nitrogen with different flow rates are blown into sensor B_i. Through analyzing the differences between the temperature measurement values of the two groups of sensors, the influence of different nitrogen flow rates on the temperature measurement value is obtained.

Fig. 6 shows the temperature values of sensor A and B_i after the temperature becomes stable. It can be seen that as the flow rate of nitrogen increases, the temperature deviation increases.

2) SIMULATION EXPERIMENT

Fig. 7 shows the temperature distribution, which is set as the initial temperature distribution of outer wall of the outer tube.

In fact, while the temperature measurement value reaches a stable state, the soot particles and soot vapor have been blown out from the inner cavity. Therefore, in addition to configuring heat conduction and convection heat transfer model, only the material properties of nitrogen, inner corundum tube and outer Al-carbon tube need to be set before simulation computing. The specific property parameters of the three materials are no longer given in details, which are fitted as the temperature-dependent functions $p = f(T)$ [10], [11].

3) VIRTUAL MODEL VERIFICATION BASED ON SIMULATION AND REAL-WORLD EXPERIMENTAL RESULTS

Through simulation, the temperature distributions of the inner wall of the cavity under different nitrogen flow rates are obtained. Fig. 8 shows the temperature distributions.

After obtaining the temperature distributions of different nitrogen flow rates, the emissivity of the whole cavity can be calculated according to the existing calculation method [3], [4], as shown in column 4 of Table 2.

Simultaneously, with the below equation, temperature measurement deviations for different temperature distributions can be calculated [5].

$$d(T_1) = \frac{T_0}{4}\varepsilon_C^{\frac{3}{4}} d\varepsilon_C \tag{42}$$

where ε_C is the emissivity of the whole cavity, and T_0 is the true temperature of the target surface.

The temperature deviations can be calculated with the cavity emissivity and target surface temperature in Table 2 by (42), as shown in column 5 of Table 2.

Comparing Fig. 6 with Table 2, it can be found that the deviation between the temperature deviation obtained by the real-world experiment and the one obtained by the simulation calculation is at most 1.4°C, which satisfies the accuracy target set in this research. In addition, according to actual use, the nitrogen flow rate is usually not higher than $2m^3$/h. Through simulation and real-world experiment, it is found that when the nitrogen flow rate is less than $2m^3$/h, $\Delta T < 0.5$°C, which meets the actual needs of the sensor.

B. VIRTUAL VERIFICATION FROM MSTime

Verification for accuracy of the virtual model from one aspect alone is not sufficiently convincing. To more effectively verify the accuracy of the virtual model, this sub-section verifies it from another perspective, i.e., the temperature MSTime.

The verification method from the perspective of temperature MSTime is shown as verification method 2. For temperature MSTime, it is mainly affected by the material properties of outer tube of the sensor. The soot impurity in the cavity is produced by the Al-carbon tube at high temperature. Due to the difference in composition of different sensor outer tubes, the amount of soot impurities generated at high temperature will also vary, resulting in difference in temperature MSTime. Therefore, the temperature measurement stability time is set to 15%.

Verification method 2	
Real-world experiment	
Setting:	Four sensors are inserted into heating furnace, and nitrogen with flow rates of 0.25 (F_1), 0.5 (F_2), 0.75 (F_3) and 1.0 (F_4) (m^3/h) are blown into the sensors, respectively.
Output:	Record temperature MSTime of the four groups of nitrogen flow rates. t_m (m=1,2,3,4)
Simulation experiment	
Setting:	Con_1, Con_2, Con_3, and Con_4 represent soot concentration under four groups of flow rate.
Output:	Deviations of MSTime between experiment and simulation $\{D_{mn}\}$ ($m \neq n$) (n=1,2,3,4).
1	For (m=1, m++, $m\leq$4)
2	{ Simulate F_m until t_m, record Con_m at this time
3	For (n=1, n++, $n\leq$4)
4	{ if ($m \neq n$)
5	{ Simulate F_n until Con_m, record t_n
6	Calculate $D_{mn}=\|t_m - t_n\|/t_m \times 100\%$
7	}
8	}
9	}
Verification	
1	If ($D_{mn(\max)}$<15%)
2	The accuracy of model is verified.
3	Else
4	The accuracy of model is not verified.

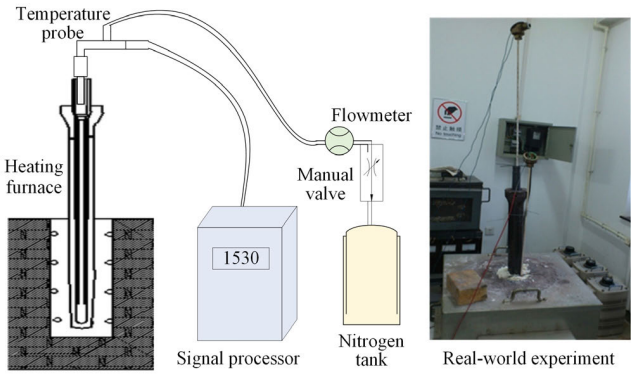

FIGURE 9. Experimental setup.

1) REAL-WORLD EXPERIMENT

In real-world experiment, as shown in Fig. 9, the insertion depth of blackbody cavity sensor is 450mm, the distance from the bottom end of the inner tube to the target surface is 390mm, and the furnace is heated to 1530°. Then nitrogen with the flow rates of 0.25, 0.5, 0.75 and 1.0 (m^3/h) is blown into the cavity. After the measurement values are stabilized, the temperature MSTime under different nitrogen flow rates are recorded. The temperature MSTime of the four groups are 120, 84, 74 and 18(s), respectively.

2) SIMULATION EXPERIMENT

The temperature at different positions of the cavity is measured by a thermocouple (only the parts inserted below the heating furnace are measured). The real-world measured temperature distribution of inner wall is used as the initial temperature distribution of the outer wall for simulation, as shown in Fig. 10. With the Step 1 in Fig. 5, the temperature distribution of the sensor is simulated. As a result, the temperature of the sensor is the same at the same height, whether it is the inner wall or outer wall of the inner tube/outer tube.

Before performing simulation, the material properties need to be set. With regard to the influence of different nitrogen flow rates on the temperature MSTime, the materials need to be considered include nitrogen, outer tube (Al-carbon), inner tube (corundum), soot particles (sodium oxide-solid) and soot vapor (sodium oxide-vapor). The properties of the five kinds of materials are fitted as the temperature-dependent functions $p = f(T)$ [6], [10], [11]. The specific physical parameters of the materials are no longer given in details.

In addition, it is necessary to initialize the concentration distribution of soot particles and soot vapor, as well as the temperature distribution of them. The fluid region of the cavity is divided into two parts of ''inner cavity-upper'' and ''inner cavity-lower'' at a phase change temperature of 1548K. The concentrations of soot particles and soot vapor are initialized at the upper and lower parts of the cavity, respectively. Meanwhile, the temperature distributions of soot particles and soot vapor need to be initialized. The initialization configuration is shown in Table 3.

3) VIRTUAL MODEL VERIFICATION BASED ON SIMULATION AND REAL-WORLD EXPERIMENT RESULTS

Through simulation, the temperature MSTime under above four groups of nitrogen flow rates are obtained and compared with the real-world experimental results.

Fig 11-(a), (b), (c) and (d) are statistically calculated based on the above-mentioned verification method 2 under the nitrogen flow rates of 0.25, 0.5, 0.75 and 1.0 (m^3/h), respectively. The regions need to be considered including the fluid region from the target surface to the bottom of inner tube and the fluid region wrapped inside the inner tube.

From Fig. 11, it can be seen that the deviation of temperature MSTime between the simulation results and the experimental results is less than 11.11%, which satisfies the target of accuracy set in this research.

Considering the virtual verification from temperature measurement accuracy and MSTime, it can be found that for the temperature measurement accuracy, the deviation between the simulation result and the real-world experimental result is less than 1.5°. And for the temperature MSTime, the deviation is less than 15%. Therefore, it can be considered that accuracy of the virtual model is successfully verified. And the setting of the boundary conditions during the simulation process is also satisfactory.

V. DESIGN IMPROVEMENT FOR BLACKBODY CAVITY SENSOR

Based on the verified virtual model, design improvement for the blackbody cavity sensor, such as optimizing the structure

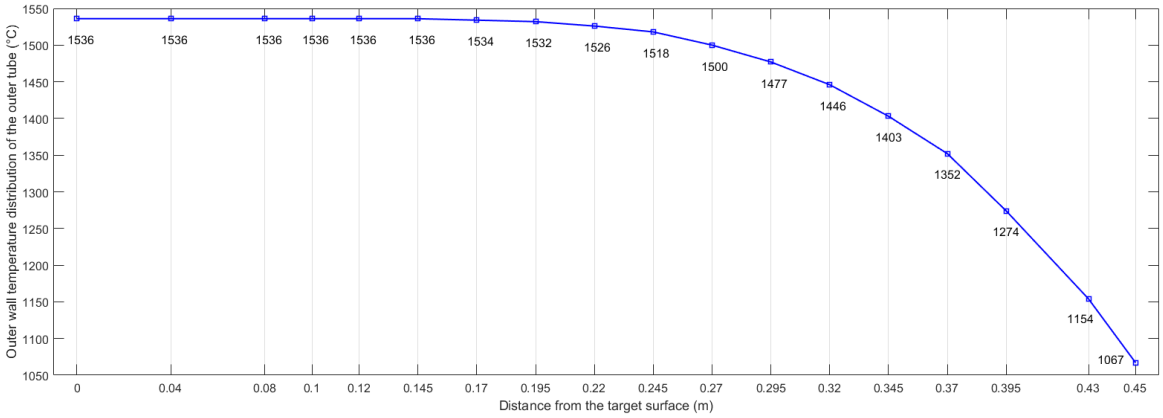

Target surface refers to the bottom end of the outer tube' inner wall.

FIGURE 10. Initial temperature distribution setting for the outer wall of the outer tube for simulation.

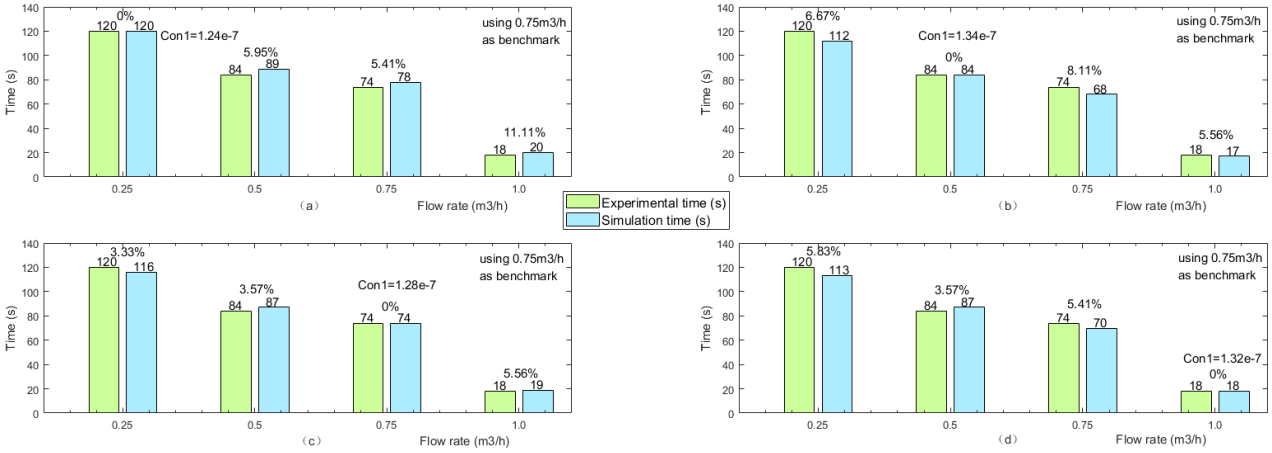

FIGURE 11. Comparison of MSTime between experiment and simulation using 0.25, 0.5, 0.75 and 1.0 (m^3/h) as the benchmark, respectively.

TABLE 3. The initialization of soot particles and vapor in cavity.

Item	Initialization region	Concentration (mol/m^3)	Temperature (K)
Soot particle	Inner cavity - upper	3.6×10^{-4}	T=1.363631×10$^5z^5$-1.990717×10$^5z^4$+9.500567×10$^4z^3$-2.25225×10$^4z^2$+2.689943×10^3z+1.681854×10^3
	Inner cavity - lower	×	×
Soot vapor	Inner cavity - upper	×	×
	Inner cavity - lower	3%	T=1.280519×10$^5z^4$-3.647827×10$^5z^3$+3.912008×10$^5z^2$-1.878365×10^5z+3.455047

parameters and nitrogen flow rates, can be carried out. For the blackbody cavity sensor, factors that may affect the flow and temperature field in the cavity include the nitrogen flow rate, the distance from the bottom of inner tube to target surface and the insertion depth of the sensor. However, the insertion depth of sensor affects temperature distribution of the outer wall, which is equivalent to the influence of the different length of the inner tube. Therefore, this section will investigate the influence of different nitrogen flow rates and inner tube's lengths on the temperature measurement accuracy and MSTime. While the influence of the two factors on the pressure distribution, velocity field, soot concentration distribution in the cavity is not given in this paper due to space limitations. In this section, the sensor insertion depth is 450 mm, and the temperature distribution of outer tube is shown in Fig. 10.

A. MSTime UNDER DIFFERENT CONDITIONS

To analyse the sensor temperature MSTime, this research uses the lowest soot concentration of 1.24×10^{-7} in the four groups of experiments in part B, Section IV as the benchmark that does not affect the temperature measurement accuracy.

The nitrogen flow rates with 0.25, 0.5, 0.75, 1.0, 1.2, 1.5 and 2.0 (m^3/h) and the distances from the bottom of inner tube to target surface with 200, 300, 390, 450 and 550 (mm) are considered in the following simulation to find the influence of temperature MSTime.

It can be found from Fig. 12 that with the same inner tube's length, as the nitrogen flow rate increases, the MSTime required for accurate temperature measurement is gradually

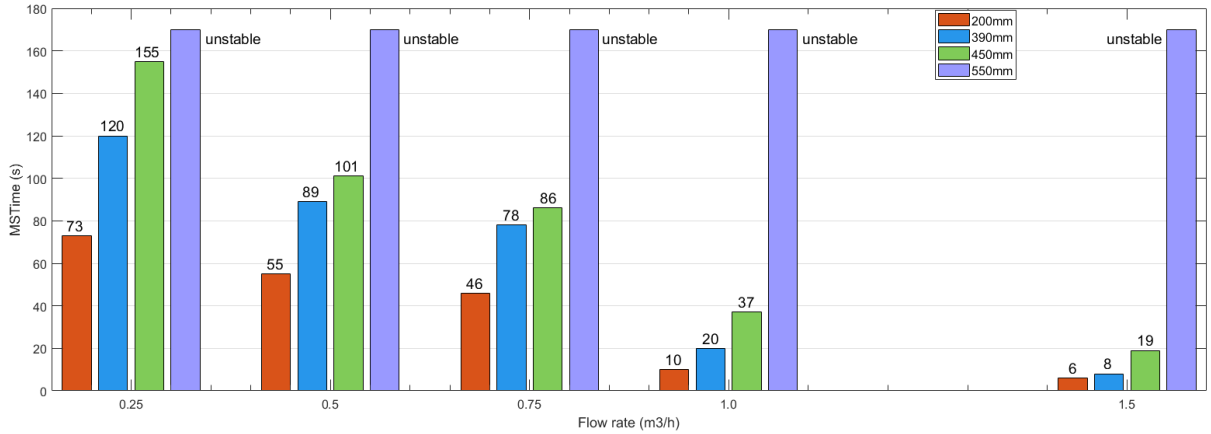

200, 390, 450 and 550 (mm) refer to the distances from the bottom of inner tube to the target surface.

FIGURE 12. MSTime at different nitrogen flow rates and inner tube' lengths (s).

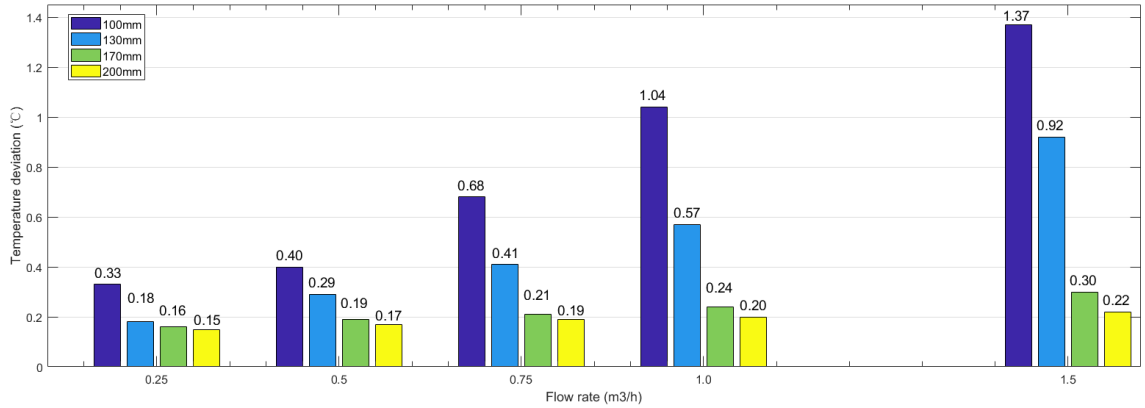

100, 130, 170 and 200 (mm) refer to the distance from the bottom of inner tube to the target surface.

FIGURE 13. The temperature deviations caused by different nitrogen flow rates and inner tube's lengths.

reduced. And in the case of the same nitrogen flow rate, as the distance from the bottom of inner tube to the target surface is farther, the MSTime required for accurate temperature measurement is gradually increased. When the distance from the bottom of inner tube to the target surface is greater than 550 mm, the temperature measurement cannot be stable for a long time.

B. TEMPERATURE MEASUREMENT ACCURACY UNDER DIFFERENT CONDITIONS

To analyze the influence of different nitrogen flow rates and different inner tube's lengths on temperature measurement accuracy and analyze the possible optimal values for practical applications, this section considers the situations of nitrogen flow rates with 0.25, 0.5, 0.75, 1.0 and 1.5 (m^3/h), and distances from the bottom of the inner tube to the target surface with 100, 130, 170 and 200 (mm). First, the emissivity (ε_{c1}) of the whole cavity can be calculated with the existing method [3], [4], as shown in Table 4.

Secondly, the reference emissivity (ε_{c0}) of whole cavity without blowing nitrogen is calculated under the distance from the bottom of inner tube to the target surface with 100, 130, 170 and 200 (mm). Then, through (42), the temperature deviation caused by blowing nitrogen can be calculated based on ε_0 and ε_1, as shown in Fig. 13.

TABLE 4. The emissivity of the whole cavity under different nitrogen flow rates and inner tube's lengths.

Emissivity (mm)	0.25 m^3/h	0.5 m^3/h	0.75 m^3/h	1.0 m^3/h	1.5 m^3/h
100	0.999261	0.999123	0.998503	0.997683	0.996959
130	0.999608	0.999366	0.999091	0.998731	0.997961
170	0.999636	0.999589	0.999533	0.999468	0.999334
200	0.999661	0.999633	0.999588	0.999564	0.999503

It can be seen from Fig. 13 that with the same inner tube's length, the larger the nitrogen flow rate is, the larger the deviation of the temperature measurement value is. In the case of the same nitrogen flow rate, as the distance from the bottom of inner tube to the target surface is closer, the deviation of the temperature measurement value is gradually increased, and vice versa. When the distance from the inner tube to the target

surface is greater than 170 mm, even if the nitrogen flow rate is increased to 1.5 m^3/h, its influence on the temperature measurement value is still weak. This is negligible compared to the temperature measurement accuracy of ±3° [3] of the blackbody cavity sensor, so it can be considered that there is no influence on the temperature measurement.

VI. CONCLUSION AND FUTURE WORK

In the process of redesign improvement, virtual model verification is one of the critical steps, which involves multidisciplinary knowledge, including materials, heat and flow science. With regard to the shortcomings of the existing blackbody cavity sensor for continuous temperature measurement of molten steel, this paper first proposes the virtual verification-based design improvement method. After redesigning the structure of the blackbody cavity sensor, the corresponding the virtual model is established. Through the comparison between real-world experiment and virtual simulation, accuracy of the virtual model is well verified. Finally, based on the verified virtual model, the design improvement has been carried out through extensive simulation, including the influence of different nitrogen flow rates and inner tube's lengths on the temperature measurement accuracy and MSTime. Thus, the major contribution of this paper is that it provides a theoretical basis and real-world test guidance for sensor design and parameter selection.

Further improvement in the accuracy of the virtual model can be achieved from the following two aspects: (1) The heat conduction and convection heat transfer model, and turbulence model are relatively accurate and do not require further improvement. However, the radiation heat transfer model, multiphase flow and interphase exchange model may need to be further improved, because the two models involve the phase change of soot impurity. Nitrogen is blown into the composite cavity under high temperature conditions, and the physical field in the cavity is more complicated. Some empirical formulas and adjustable parameters are involved. This research work may not be able to adjust all parameters to the optimal values. Therefore, the related models established in this article may have room for further improvement. (2) Another factor is the accuracy of solution computation, mainly including mesh size, mesh quality, and iterative solution step size.

REFERENCES

[1] G. Mei, J. Zhang, X. Wang, S. Zhao, and Z. Xie, "Spectral and total effective emissivity of a nonisothermal blackbody cavity formed by two coaxial tubes," *Appl. Opt.*, vol. 54, no. 13, pp. 3948–3955, May 2015.

[2] G. Mei, J. Zhang, S. Zhao, and Z. Xie, "Effective emissivity of a blackbody cavity formed by two coaxial tubes," *Appl. Opt.*, vol. 53, no. 11, pp. 2507–2514, Apr. 2014.

[3] Z. Xie, Y. Ci, H. Meng, and H. Zhang, "Development of continuous temperature measuring sensor for liquid steel based on blackbody cavity," *Chin. J. Sci. Instrum.*, vol. 26, no. 5, pp. 446–448, May 2005.

[4] Y. Ci, Z. Xie, and H. Zhang, "New approach to continuous temperature measurement of liquid steel in CC tundish," *J. Northeastern Univ. Natural Sci.*, vol. 25, no. 5, pp. 460–462, May 2004.

[5] J. Cheng, C.-F. Juang, W. Chen, and G. Mei, "Axiomatic design and virtual verification for blackbody cavity sensor," in *Proc. Matec Web Conf.*, vol. 301, Dec. 2019, p. 00022.

[6] *NIST-JANAF Thermochemical Tables. 1313-59-3 Sodium Oxide*. Accessed: Aug. 1, 1998. [Online]. Available: http://kinetics.nist.gov/janaf

[7] R. W. Hedrick and R. J. Urbanic, "Integration of additive manufacturing and virtual verification strategies within a commercial CAM system," *Comput.-Aided Des. Appl.*, vol. 10, no. 4, pp. 567–583, Aug. 2013.

[8] M. C. Leu, H. A. ElMaraghy, A. Y. C. Nee, S. K. Ong, M. Lanzetta, M. Putz, W. Zhu, and A. Bernard, "Cad model based virtual assembly simulation, planning and training," *CIRP Ann. Manuf. Technol.*, vol. 62, no. 2, pp. 799–822, 2013.

[9] S. V. Patankar, and Z. Zhang, *Numerical Calculation Of Heat Transfer And Fluid Flow*. Beijing, China: Science Press, 1984, pp. 17–19.

[10] Y. Ma, and R. Fang, *Practical Thermophysical Properties Handbook*. Beijing, China: Machine Press, 1986, pp. 109–131.

[11] J. Zhang, *Handbook of Thermophysical Properties of Commonly Used Materials*. Beijing, China: New Times Press, 1987, pp. 256–261.

[12] W. Fiveland, A. Jamaluddin, and J. Thermophys, "Three-dimensional spectral radiative heat transfer solutions by the discrete-ordinates method," *J. Thermophys. Heat Transf.*, vol. 5, pp. 335–339, Jul./Sep. 1991.

[13] G. D. Raithby and E. H. Chui, "A finite volume method, for predicting a radiant heat transfer in enclosures with participating media," *J. Heat Transf.*, vol. 112, pp. 415–423, May 1990.

[14] X. Lu and T. Wang, "Investigation of radiation models in entrained-flow coal gasification simulation," *Int. J. Heat Mass Transf.*, vol. 67, pp. 377–392, Dec. 2013.

[15] W. A. Fiveland, "Three-dimensional radiative heat-transfer solutions by the discrete-ordinates method," *J. Thermophys. Heat Transf.*, vol. 2, pp. 309–316, Oct. 1988.

[16] E. H. Chui and G. D. Raithby, "Computation of radiant heat transfer on a nonorthogonal mesh using the finite-volume method," *Numer. Heat Transf. B, Fundamentals*, vol. 23, pp. 269–288, Apr./May 1993.

[17] S. A. Orszag, V. Yakhot, W. S. Flannery, F. Boysan, D. Choudhury, J. Maruzewski, and B. Patel, "Renormalization group modeling and turbulence simulations," in *Proc. Int. Conf. Near-Wall Turbulent Flows*, Tempe, Arizona, 1993, pp. 187–199.

[18] B. E. Launder, and D. B. Spalding, *Lectures in Mathematical Models of Turbulence*. New York, NY, USA: Academic, 1972.

[19] V. Yakhot and S. A. Orszag, "Renormalization group analysis of turbulence. I. Basic theory," *J. Sci. Comput.*, vol. 1, no. 1, pp. 1–51, Mar. 1986.

[20] M. Hassanizadeh and W. G. Gray, "General conservation equations for multi-phase systems: 3. Constitutive theory for porous media flow," *Adv. Water Resour.*, vol. 3, no. 1, pp. 25–40, Mar. 1980.

[21] W. Sobieski, "Momentum exchange in solid-fluid system modeling with the Eulerian multiphase model," *Dry. Technol.*, vol. 27, no. 5, pp. 653–671, Apr. 2009.

[22] J. J. Monaghan and A. Kocharyan, "SPH simulation of multi-phase flow," *Comput. Phys. Commun.*, vol. 87, nos. 1–2, pp. 225–235, May 1995.

[23] N. I. Kolev, *Multiphase Flow Dynamics 2: Thermal and Mechanical Interactions*. Berlin, Germany: Springer, 2005.

[24] M. Syamlal and T. J. O'Brien, "Computer simulation of bubbles in a fluidized bed," *AIChE Symp. Ser.*, vol. 85, no. 1, pp. 22–31, Jan. 1989.

[25] L. Schiller and A. Naumann, "Fundamental calculations in gravitational processing," *Z. Ver Deut. Ing.*, vol. 77, nos. 318–320, 1933.

[26] C. K. K. Lun, S. B. Savage, D. J. Jeffrey, and N. Chepurniy, "Kinetic theories for granular flow: Inelastic particles in Couette flow and slightly inelastic particles in a general flowfield," *J. Fluid Mech.*, vol. 140, pp. 223–256, Mar. 1984.

[27] D. Gidaspow, R. Bezburuah, and J. Ding, "Hydrodynamics of circulating fluidized beds: Kinetic theory approach," in *Proc. 7th Fluidization*, May 1992, pp. 75–82.

[28] M. Syamlal, W. Rogers, and T. J. O'Brien, *MFIX Documentation: Volume 1, Theory Guide*. Springfield, VA, USA: National Technical Information Service, 1993.

[29] W. E. Ranz and W. R. Marshall, "Evaporation from drops," *Chem. Eng. Prog.*, vol. 48, no. 3, pp. 173–180, Apr. 1952.

JIANGFENG CHENG received the B.S. degree in automation engineering from Qufu Normal University, Rizhao, China, in 2011, and the M.S. degree in measurement technology and automation equipment from Northeastern University, Shenyang, China, in 2013. He is currently pursuing the Ph.D. degree with Beihang University, Beijing, China, and National Chung-Hsing University, Taichung, Taiwan.

His current research interests include cyber-physical manufacturing systems, digital twin driven product design, manufacturing and service, smart interconnection in digital manufacturing shop-floor, and service-oriented smart manufacturing.

CHIA-FENG JUANG (M'99–SM'08-F'19) received the B.S. and Ph.D. degrees in control engineering from National Chiao-Tung University, Hsinchu, Taiwan, in 1993 and 1997, respectively. Since 2001, he has been with the Department of Electrical Engineering, National Chung Hsing University (NCHU), Taichung, Taiwan, where he became a Full Professor, in 2007, and has been a Distinguished Professor, since 2009. He has authored or coauthored seven book chapters, over 90 journal articles (including over 55 IEEE journal articles), and over 100 conference papers. His current research interests include computational intelligence, intelligent control, computer vision, and evolutionary robots. He was elevated to CACS Fellow, in 2016. He received the Outstanding Youth Award from Taiwan System Science and Engineering Society, Taiwan, in 2010, the Excellent Research Award from NCHU, Taiwan, in 2010, the Outstanding Youth Award from Taiwan Fuzzy Systems Association, Taiwan, in 2014, and the Outstanding Automatic Control Engineering Award from Chinese Automatic Control Society (CACS), Taiwan, in 2014. He is an Associate Editor of the IEEE TRANSACTIONS ON FUZZY SYSTEMS, the IEEE TRANSACTIONS ON CYBERNETICS, *Asian Journal of Control*, and *Journal of Information Science and Engineering*, and an Area Editor of *International Journal of Fuzzy Systems*.

GUOHUI MEI received the B.S. degree in mechanical manufacture from the Shenyang University of Technology, Shenyang, in 1995, the M.S. degree in mechanical design and theory from Dalian Polytechnic University, Dalian, in 1998, and the Ph.D. degree in mechanical design and theory from Northeastern University, Shenyang, in 2001. He was an Associate Professor with Northeastern University, in 2005. His current research interest includes infrared radiation temperature measuring theory and technology. He received the second prize of the National Technology Invention, China, in 2005.

WEIHAI CHEN (M'00) received the B.S. degree in detection technology from Zhejiang University, Hangzhou, China, in 1982, and the M.S. and Ph.D. degrees in mechanical engineering from Beihang University, Beijing, China, in 1988 and 1996, respectively. He was an Associate Professor, in 1999, and a Professor, in 2007, with Beihang University, where he is currently the Director of the Intelligent Robotics and Measurement and Control Technology Laboratory. His research interests include bioinspired robotics, micromanipulation, and computer vision. He is a member of the Technical Committee on Manufacturing Automation of the IEEE Robotics and Automation Society and a Senior Member of the Chinese Mechanical Engineering Society.